

# **Quantum materials for spin to charge conversion**

Dissertation

zur Erlangung des akademischen Grades

Doktor-Ingenieur (Dr.-Ing.)

der Naturwissenschaftlichen Fakultaet II

Chemie, Physik und Mathematik

der Martin-Luther-Universitaet Halle-Wittenberg

vorgelegt von Herrn

**Avanindra Kumar Pandeya**

geb. am Muzaffarpur, India

Gutachter :

Prof. Dr. Stuart S. P. Parkin

Tag der mündlichen Prüfung:



# **Zusammenfassung**



## **Abstract**



# Acknowledgements

I would like to thank Prof Stuart Parkin for the opportunity to undertake my doctoral studies under his supervision, and for his valuable expertise and guidance during my time at the Max Planck Institute of Microstructure Physics. Here, my gratitude goes to the many other scientists and students, foremost Edouard Lesne, for their advice and encouragement in my development as a scientist: Fasil Kidane Dejene, Kumari Gaurav Rana, Neeraj Kumar, Peter Werner, Hakan Deniz, Hoelger Meyerheim, Robin Blaesing, Pranava Keerthi Sivakumar, Elisa Yang, Amilcar Bedoya Pinto, Avanindra Kumar Pandeya, Tianping Ma, Bharat Grover, Binoy Krishna Hazra, Banabir Pal, Hao Yang, Jue Huang, Yicheng Guan, Ankit Kumar Sharma, Abhay Kant Srivastava, Jibo Zhang, Jae-Chun Jeon, Andrea Migliorini, Kai-Uwe Demasius, Elena Derunova, Mazhar Ali, Amir Capua, Rana Saha, Bin Cui, Fang Gao, Ajaya Nayak, Ilya Kostanovski and, of course, Jiho Yoon, Alessandro Fumarola and Amine Wahada. For technical assistance, I heartily acknowledge Kai-Uwe Assmann, Kornelia Sklarek, Martin Gottschalk, Norbert Schammelt, Mike Borrmann and Pierre-Jean Zermattan, as well as the wisdom of Winfried Heichler. For administrative help over the last few years, my thanks go to Antje Paetzold and Simone Jaeger.



# **Contents**

*The story so far: In the beginning the Universe was created. This has made a lot of people very angry and been widely regarded as a bad move.*

Douglas Adams

# 1

## Introduction

### 1.1 Moore's Law – Room at the bottom is shrinking

The number of transistors per unit area in electronic circuit keeps doubling almost every two years. It was first observed by Gordon Moore in his 1965 paper. In many ways Moore's law has been surpassed so far. Aggressive scaling of electronic devices which has followed Moore's law has made "plenty of room" for storage and devices as Feynman had once envisaged in his famous lecture. But pace of growth is plateauing and there is a limit to where CMOS can take us.

Memory devices have similarly experienced a lot of growth due to scaling but we are reaching the limits of what can be achieved. The main form in which data is stored is magnetic bits and these bits are read and written using magnetic read/write head.

### 1.2 Spintronics for scaling and beyond

The key to achieving this is making sure that any internal status of computation is stored before power is turned off, without consuming power. Non-volatile RAM is therefore a critical component. It offers an infinite number of fast write and read operations as well as non-volatility. Furthermore, this memory is free of soft-errors caused by radiation. Spin-transfer torque RAM

### **1.3 Quantum materials for spintronics**

Nominally highly spin-polarized materials, as discussed in the previous sections, could provide both effective spin injection into nonmagnetic materials and large magnetoresistance effects, important for nonvolatile applications. Examples include half-metallic oxides such as CrO<sub>2</sub>, Fe<sub>3</sub>O<sub>4</sub>, CMR materials, and double perovskites. Most of the currently studied ferromagnetic semiconductors are p-doped with holes as spin-polarized carriers, which typically leads to lower mobilities and shorter spin relaxation times than in n-doped materials. It is possible to use selective doping to substantially increase T<sub>c</sub>, as compared to the uniformly doped bulk ferromagnetic semiconductors.

### **1.4 Dichalcogenides**

Graphene is not the only prominent example of two-dimensional (2D) materials. Due to their interesting combination of high mechanical strength and optical transparency, direct bandgap and atomic scale thickness transition-metal dichalcogenides (TMDCs) are an example of other materials that are now vying for the attention of the materials research community. In this article, the current state of quantum-theoretical calculations of the electronic and mechanical properties of semiconducting TMDC materials are presented. In particular, the intriguing interplay between external parameters (electric field, strain) and band structure, as well as the basic properties of heterostructures formed by vertical stacking of different 2D TMDCs are reviewed. Electrical measurements of MoS<sub>2</sub>, WS<sub>2</sub>, and WSe<sub>2</sub> and their heterostructures, starting from simple field-effect transistors to more demanding logic circuits, high-frequency transistors, and memory devices, are also presented.

### **1.5 Weyl semi-metals**

Weyl semimetals are semimetals or metals whose quasiparticle excitation is the Weyl fermion, a particle that played a crucial role in quantum field theory but has not been observed as a fundamental particle in vacuum<sup>1-24</sup>. Weyl fermions have definite chiralities, either left-handed or right-handed. In a Weyl semimetal, the chirality can be understood as a topologically protected chiral charge. Weyl nodes of opposite chirality are separated in momentum space and

are connected only through the crystal boundary by an exotic non-closed surface state, the Fermi arcs. Remarkably, Weyl fermions are robust while carrying currents, giving rise to exceptionally high mobilities. Their spins are locked to their momentum directions, owing to their character of momentum-space magnetic monopole configuration. Because of the chiral anomaly, the presence of parallel electric and magnetic fields can break the apparent conservation of the chiral charge, making a Weyl metal, unlike ordinary nonmagnetic metals, more conductive with an increasing magnetic field. These new topological phenomena beyond topological insulators make new physics accessible and suggest potential applications, despite the early stage of the research

## 1.6 Outline

The thesis is organized as follows:

- Chapter 2 discusses the theoretical background required to understand spin to charge conversion and the methods required to measure them
- Chapter 3 discusses the experimental set up used to perform the experiments
- Chapter 3 discusses growth and characterization of  $\text{NbSe}_2$
- Chapter 4 discusses the growth and characterization of weyl semimetals
- Chapter 5 discusses the electrical properties of dichalcogenides and WSMs
- Chapter 6 discusses the spin-tocharge conversion in WSMs and dichalcogenides



# 2

## Spintronics and Quantum Materials

### 2.1 Spin current - Two current model

At a very basic level, spin current if net transfer of spins from one point to another. Spin Current is actually defined as a tensor  $q_{ij}$ , where  $i$  denotes the direction of flow of spin current and  $j$  denotes the which component of spin is flowing[7]. The indices  $i$  and  $j$  are the directions in the 3D space. We can, in principle, have an net spin current without any flow of charge current, if equal amount of up and down electron are moving in opposite direction. That is why these are often touted as dissipationless[8]. But in reality, one always needs some amount of charge current to create the spin current in the first place which should be taken into consideration for making a fair comparison.

There can be a net spin current if there is an imbalance between the up spin and down spin flowing in the opposite direction to each other. Let us define electrical spin polarization  $P_j$  in the direction  $j$  as follows:

$$P_j = \frac{n^\uparrow - n^\downarrow}{n^\uparrow + n^\downarrow} \quad (2.1)$$

??

### 2.2 How to create spin current?

We can create spin current using many methods. One of the most simple methods is to take a ferromagnet and pass current through it and inject the

current coming out of the ferromagnet into wherever we might need[9]. But this is a fairly inefficient method. There are other methods like spin pumping, spin Hall effect and inverse spin galvanic effect (Rashba-Edelstein effect) etc. Let us discuss these methods in detail.

## 2.3 How to measure spin current?

Future spintronic circuits will use the spin orientation of an electron current to store and manipulate information. Such spin-polarized currents, however, cannot be directly observed and are typically characterized using indirect techniques. Zi Qiu at the University of California, Berkeley, and colleagues have now demonstrated that x-ray pulses from a synchrotron source can be used to measure the precession of spins in a material, which directly reveals the flow of a spin current. The technique allowed the researchers to observe a spin current as it propagated through different layers of materials.

Spin currents are generally probed using measurements of the effects they produce in the metals through which they flow. They can, for instance, create a voltage drop perpendicular to the direction of the spin current or a torque that turns the magnetization direction of a magnetic film. However, these indirect measurements are often ambiguous because they are influenced by factors other than the spin current, such as magnetic proximity effects.

## 2.4 Landau-Lifshitz-Gilbert Equation

The magnetization of a sample experiences a torque perpendicular to the direction of applied field and the direction of magnetization. In absence of any damping the magnetization can keep precessing around the applied field forever. But in real materials the radius of precession keeps decreasing and eventually all the magnetizations point towards the applied magnetic field.

$$\dot{\mathbf{M}} = -\gamma(\mathbf{M} \times \mathbf{H}) + \frac{\alpha}{M} (\mathbf{M} \times \dot{\mathbf{M}}) \quad (2.2)$$

## 2.5 Spin-Torque Ferrromagnetic Resonance - STFMR

When a dc magnetic field  $H_{ext}$  is swepted in the STFMR configuration, the mixing voltage [10], can be expressed as in ??:

$$V_{mix} = V_0 + V_{sym} \frac{\Delta H^2}{\Delta H^2 + (H_{ext}^2 + H_{res}^2)} + V_{as} \frac{\Delta H (H_{ext} - H_{res})}{\Delta H^2 + (H_{ext}^2 + H_{res}^2)} \quad (2.3)$$

We fit this equation to extract fitting parameters  $V_0$ ,  $H_{res}$ ,  $V_{sym}$ ,  $V_{as}$ ,  $H_{res}$ , and  $\Delta$ . When there is no DC current passing through the metal layer, the resonance field can be used to fit effective magnetization using Kittel formula [11] using ??.

$$f_{res} = \frac{\gamma}{4\pi} \sqrt{(H_{res} + H_0)(H_{res} + H_0 + M_{eff})} \quad (2.4)$$

The Gilbert damping can be extracted from the linewidth of the resonance peak [11] using equation ??.

$$\Delta H = \Delta H_{res} + \frac{2\pi f}{\lambda} \alpha \quad (2.5)$$

When a dc current is passed through the normal metal it pumps spin current into the ferromagnetic layer. In presence of a spin current the equation (4) is modified as [12], [13]:

$$\Delta H = \Delta H_{res} + \frac{2\pi f}{\lambda} \left( \alpha + \frac{\sin \phi}{(H_{ext} + 0.5M_{eff})\mu_0 M_{st}} \frac{\hbar}{2e} J_s \right) \quad (2.6)$$

The change in linewidth ( $\delta\Delta H$ ) for two different values of spin current ( $\Delta J_s = J_{s1} - J_{s2}$ ) will be:

$$\delta\Delta H = \frac{2\pi f}{\lambda} \left( \alpha + \frac{\sin \phi}{(H_{ext} + 0.5M_{eff})\mu_0 M_{st}} \frac{\hbar}{2e} J_s \right) \quad (2.7)$$

The ?? can be rearranged to get an expression of  $\Delta J_s$ :

$$\Delta J_s = \frac{\delta\Delta H}{\frac{2\pi f}{\lambda} \left( \alpha + \frac{\sin \phi}{(H_{ext} + 0.5M_{eff})\mu_0 M_{st}} \frac{\hbar}{2e} J_s \right)} \quad (2.8)$$

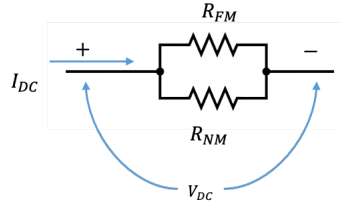


**Fig. 2.1:** Parallel connection between the ferromagnetic and normal metal layer

We can assume a simple model of parallel connection between the ferromagnetic layer and the normal metal layer to find out the current distribution within the bilayer.

The current density through the metal layer is calculated as follows:

$$J_{NM} = \frac{I_{NM}}{A_c} = \frac{V_{DC}/R_{NM}}{A_C} = I_{DC} \frac{R_{FM}R_{NM}}{R_{FM} + R_{NM}} \frac{1}{R_{NM}A_C} \quad (2.9)$$

$$\implies J_{NM} = I_{DC} \frac{R_{FM}}{(R_{FM} + R_{NM})A_C} \quad (2.10)$$

$$\implies \Delta J_{NM} = \Delta I_{DC} \frac{R_{FM}}{(R_{FM} + R_{NM})A_C} \quad (2.11)$$

Using ?? and ?? , we have

$$\theta = \frac{\Delta J_{NM}}{\Delta J_S} \quad (2.12)$$

$$\implies \theta = \frac{\delta \Delta I_H / \delta \Delta I_{DC}}{\frac{2\pi f}{\lambda} \left( \alpha + \frac{\sin \phi}{(H_{ext} + 0.5M_{eff})\mu_0 M_{st}} \frac{\hbar}{2e} J_s \right)} \frac{R_{FM}}{(R_{FM} + R_{NM})} A_C \quad (2.13)$$

This is the final relation which we use to calculate the Spin-Hall ratio in our experiments.

## 2.6 Second Harmonic Hall

Let us take a hall bar of NM-FM heterostructure and pass ac current ( $I_0 \sin \omega t$ ) through it in presence of an in-plane magnetic field ( $B_0$ ) and measure transversal

## 2.6 Second Harmonic Hall

voltage ( $V_{xy}(t)$ ) across it. The effective magnetic field acting on the sample will have both ac and dc components:

$$\mathbf{B} = \mathbf{B}_{\text{DC}} + \mathbf{B}_{\text{ac}}(\mathbf{t}) \quad (2.14)$$

where,

$$\mathbf{B}_{\text{DC}} = \mathbf{B}_0 + \mathbf{B}_{\text{ani}} \quad (2.15)$$

$$\mathbf{B}_{\text{ac}(\mathbf{t})} = \mathbf{B}_{\text{AD}} + \mathbf{B}_{\text{FL}} + \mathbf{B}_{\text{Oe}} = \mathbf{b} \sin \omega t \quad (2.16)$$

$$V_{xy}(t) = R_{xy}(t) \times I_0 \sin \omega t \quad (2.17)$$

$$R_{xy}(t) = R_{xy}(\mathbf{B}_{\text{DC}}) + \frac{\partial R_{xy}}{\partial \mathbf{B}_{\text{ac}}} \mathbf{b} \sin \omega t \quad (2.18)$$

$$V_{xy}(t) = \left( R_{xy}(\mathbf{B}_{\text{DC}}) + \frac{\partial R_{xy}}{\partial \mathbf{B}_{\text{ac}}} \mathbf{b} \sin \omega t \right) I_0 \sin \omega t \quad (2.19)$$

$$V_{xy}(t) = R_{xy}(\mathbf{B}_{\text{DC}}) I_0 \sin \omega t + \frac{\partial R_{xy}}{\partial \mathbf{B}_{\text{ac}}} I_0 \mathbf{b} \sin^2 \omega t \quad (2.20)$$

$$V_{xy}(t) = R_{xy}(\mathbf{B}_{\text{DC}}) I_0 \sin \omega t + \frac{\partial R_{xy}}{\partial \mathbf{B}_{\text{ac}}} I_0 \mathbf{b} \left( \frac{1 - \cos 2\omega t}{2} \right) \quad (2.21)$$

$$V_{xy}(t) = R_{xy}(\mathbf{B}_{\text{DC}}) I_0 \sin \omega t + \frac{1}{2} \frac{\partial R_{xy}}{\partial \mathbf{B}_{\text{ac}}} I_0 \mathbf{b} - \frac{1}{2} \frac{\partial R_{xy}}{\partial \mathbf{B}_{\text{ac}}} I_0 \mathbf{b} \cos 2\omega t \quad (2.22)$$

$$V_{xy}(t) = R_{xy}^0 I_0 + R_{xy}^\omega I_0 + R_{xy}^{2\omega} I_0 \quad (2.23)$$

Comparing ?? and ??, we get:

$$R_{xy}^0 = \frac{1}{2} \frac{\partial R_{xy}}{\partial \mathbf{B}_{ac}} \mathbf{b} \quad (2.24)$$

$$R_{xy}^\omega = R_{xy}(\mathbf{B}_{DC}) \sin \omega t \quad (2.25)$$

$$R_{xy}^{2\omega} = -\frac{1}{2} \frac{\partial R_{xy}}{\partial \mathbf{B}_{ac}} \mathbf{b} \cos 2\omega t \quad (2.26)$$

This means that the first harmonic amplitude is exactly like the Dc measurement which will have AHE and PHE effect contributions[14]:

The second harmonic signal has three major source contributions:

1. Contribution due to Oerested Field
2. Contribution due to torque on the magnetization of FM due to the spin current from the NM
3. ontribution due to the thermal gradient along the substrate to the top layer of the film

The second harmonic expression for transverse resistance can be written as:

$$\begin{aligned} R_{xy}^{2\omega} = & (R_{AHE} - 2R_{PHE} \cos \theta \sin 2\phi) \frac{\partial \cos \theta}{\partial \theta_B} \frac{B_{ac}^\theta}{B_0 \cos(\theta_B - \theta)} \\ & + R_{PHE} \sin^2 \theta \frac{\partial \sin 2\phi}{\partial \phi_B} \frac{B_{ac}^\phi}{\sin \theta_B \sin(\theta_B - \theta) B_0} \\ & + \alpha \nabla T I_0 \sin \theta \cos \phi \end{aligned} \quad (2.27)$$

When the field is applied in-plane of the sample  $\theta_B = \pi/2$  and for permalloy with PMA,  $\theta \approx \pi/2$ , and  $\phi_B \approx \phi$  above equation can be simplified to:

$$R_{xy}^{2\omega} = R_{AHE} \frac{\partial \cos \theta}{\partial \theta_B} \frac{B_{ac}^\theta}{B_0} + R_{PHE} \frac{\partial \sin 2\phi}{\partial \phi_B} \frac{B_{ac}^\phi}{B_0} + \alpha \nabla T I_0 \sin \theta \cos \phi \quad (2.28)$$

## 2.6 Second Harmonic Hall

Calculating the derivatives at the above mentioned angles, we get,

$$R_{AHE} \frac{\partial \cos \theta}{\partial \theta_B} = R_{AHE} \sin \theta \partial \theta \theta_B = R_{AHE} \quad (2.29)$$

$$R_{PHE} \frac{\partial \sin 2\phi}{\partial \phi_B} = R_{PHE} 2 \cos 2\phi = R_{PHE} (\cos^2 \phi - 1) \quad (2.30)$$

Substituting these values from ?? and ?? into ?? we get,

$$R_{xy}^{2\omega} = R_{AHE} \frac{B_{ac}^\theta}{B_0} + R_{PHE} (\cos^2 \phi - 1) \frac{B_{ac}^\phi}{B_0} + \alpha \nabla T I_0 \sin \theta \cos \phi \quad (2.31)$$

The antidumping and field like torques are given by:

$$\mathbf{B}_{AD} = B_{AD} (\mathbf{m} \times \mathbf{y}) = B_{AD} \cos \phi \hat{\theta} \quad (2.32)$$

$$\mathbf{B}_{FL+Oe} = (B_{FL} + B_{Oe}) (\mathbf{m} \times \mathbf{m} \times \mathbf{y}) = (B_{FL} + B_{Oe}) \cos \phi \hat{\phi} \quad (2.33)$$

Substituting these values from ?? and ?? in the expression for second harmonic resistance in ?? we get,

$$R_{xy}^{2\omega} = R_{AHE} \frac{B_{AD} \cos \phi}{B_0} + R_{PHE} (\cos^2 \phi - 1) \frac{(B_{FL} + B_{Oe})}{B_0} + \alpha \nabla T I_0 \sin \theta \cos \phi \quad (2.34)$$

$$R_{xy}^{2\omega} = \left[ \left( R_{AHE} \frac{B_{AD}}{B_0} + \alpha \nabla T I_0 \right) \cos \phi + 2R_{PHE} (\cos^3 \phi - \cos \phi) \frac{(B_{FL} + B_{Oe})}{B_0} \right] \quad (2.35)$$

The simulation of the above equation gives following result.

The raw data is symmetrized before fitting to get rid of unwanted contributions due to misalignment of Hall branches, or misalignment of sample with respect to external fields. The odd part of the second harmonic signal and the even part of the first harmonic signal is taken before fitting the data.



# 3

## Experimental Set Up

### 3.1 PAPAYA

PAPAYA is growth-cum-analysis chamber which allows users to grow samples using MBE and characterize them using various in-situ techniques. It has 3 MBE chambers, an XPS chamber and a low temperature STM-cum-Q plus AFM. The system have following features:

1. Selenide MBE : We can grow various Metal Selenide in this chamber. It's one port has Se and has 4 ports for other metals like Nb, Pd, V etc. The substrate can rotate up to 320°C and heated up to 900°C The chamber has RHEED for characterizing the thin film while growing it.
2. Telluride MBE: Various Tellurides can be grown in this chamber. It has only 3 ports and has mateials like SnTe in it. It has not been used in this work and hence, will not be described in detail here.
3. Metal MBE: Despite its name we can grow both metals and non-metals in it. It has 5 ports and Al, MgO, Py (Ni80Fe20), Ni and Cu can be grown in this chamber. The sample can rotated for 360°C but can be heated and hence, everything is grown at room temperature.
4. In-Situ X-ray photoelectron spectra (XPS) system: XPS is a surface sensitive techinique which can be used to characterize the elemental composition of a material and chemical states of these elements. It is a standard characterization tool based of photoelectric effect. When X-Ray with energy

### Chapter 3 Experimental Set Up

( $E_{photon}$ ) with falls on a material with electron with binding energy ( $E_{binding}$ ) and surface work function ( $\phi$ ), electrons with energy ( $E_{kinetic}$ ) are emitted.

$$E_{binding} = E_{photon} - (E_{kinetic} + \phi) \quad (3.1)$$

The kinetic energy of the emitted electrons is measured using a hemispherical analyser and using the ?? we can estimate the binding energy of the electrons. The XPS spectrum is number of detected electrons as a function of binding (or kinetic energy). A peak is observed corresponding to the binding energies of the electrons present in an element. Every element has electrons at fixed binding energies and thus, a set of peaks can serve as a fingerprint of the element. The position of the peaks may increase or decrease by a little bit based on its chemical state. The relative concentration of various elements can be estimated by taking the ratio of area under the curve of these peaks after taking relative sensitivity factor into account and subtracting background properly.

$$\frac{C_1}{C_2} = \frac{A_1 \times r_2}{A_2 \times r_1} \quad (3.2)$$

An omicron machine with Al and Mg sources is attached to PAPAYA. The measurements can be done only at room temperature in this system.

5. In-Situ Scanning Tunneling Microscope (STM): The STM experiments were performed on an Omicron VT-STM-XT system operated at room temperature with a base pressure of  $2 \times 10^{-11}$  mbar. The mechanically sharpened Pt/Ir tips were treated and checked on Au(111) surface before measurements, and the topography images were acquired at room-temperature.

## 3.2 TAMARIND - Topological materials engineering by epitaxial design

It can be used to phosphides and arsenides. It has 7 ports in which Nb, Ta, Py, MgO, GaP (as source of P) and GaAs (as source of As) is attached. The

### 3.3 STFMR Set-Up

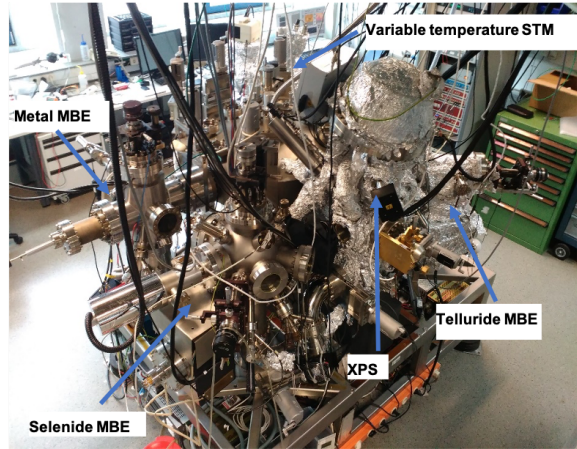


**Fig. 3.1:** PAPAYA System

substrate can be rotated up to 320 ° and heated up to 1200 °C using resistive heating. To achieve higher substrate temperature there is a possibility to use e-beam heating. The substrate can be cooled using liquid N<sub>2</sub> to up to -30 °C. There is a RHEED to monitor the growth of the film. There is a residual gas analyser and a mass spectrometer to monitor the partial pressure of various gaseous species in the chamber.

## 3.3 STFMR Set-Up

## 3.4 Second Harmonic Hall Set Up

### Chapter 3 Experimental Set Up

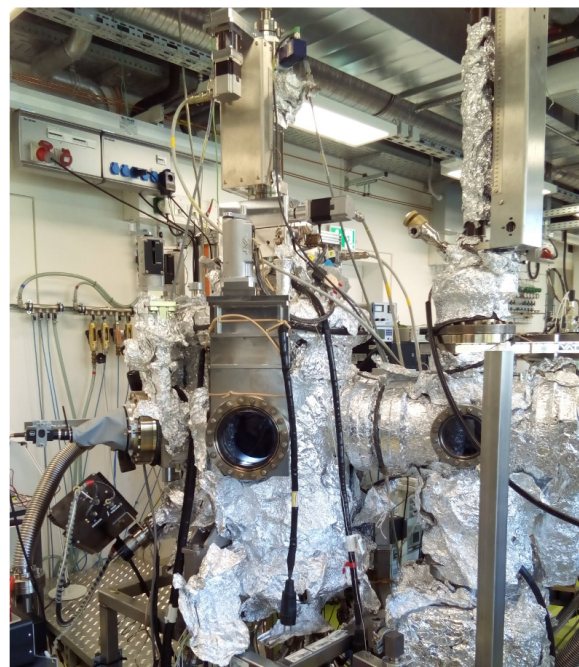


**Fig. 3.2:** TAMRAIND System

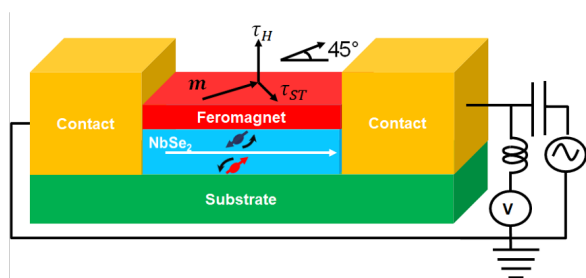


**Fig. 3.3:** STFMR Schematic

# 4

## Growth and Characterization of NbSe<sub>2</sub>

NbSe<sub>2</sub> samples in this study were grown using Molecular beam epitaxy (MBE) on c-plane of sapphire substrate from Crystec. The substrate was cleaned using modified RCA method as described in ?? and loaded in the selenide chamber of PAPAYA where it was degassed at 700°C for about 1 hour. Nb and Se are co evaoparoated from e-beam and K-cells respectively such that ther flux ratio is 1:20. The first 3 monolayers (ML) were grown at 570°C and all the subsequent layers were grown at 650°C. The deposited sample was annealed at 700°C for the first time after deposition of 3 ML and then intermittently after every 10-15 MLs. The growth is monitored continuously using RHEED and the stoichiometry and morphology is assessed intermittently using XPS and STM respectively. Once the sample is taken out of the chamber its structure is assessed using XRD and Raman.

### 4.1 Cleaning Al<sub>2</sub>O<sub>3</sub> substrate

The substrates which we receive from the suppliers usually have both metallic and organic impurities on them. The AFM of the substrate as received from the supplier is shown in ?? The recipe for cleaning the substrate is as follows:

1. Soak the substrate in ethanol for 12 hours.
2. Clean the substrate in ultrasonic bath of acetone and Isopropanol for 5 minutes each to remove bulky dissolvable contaminants and particulates

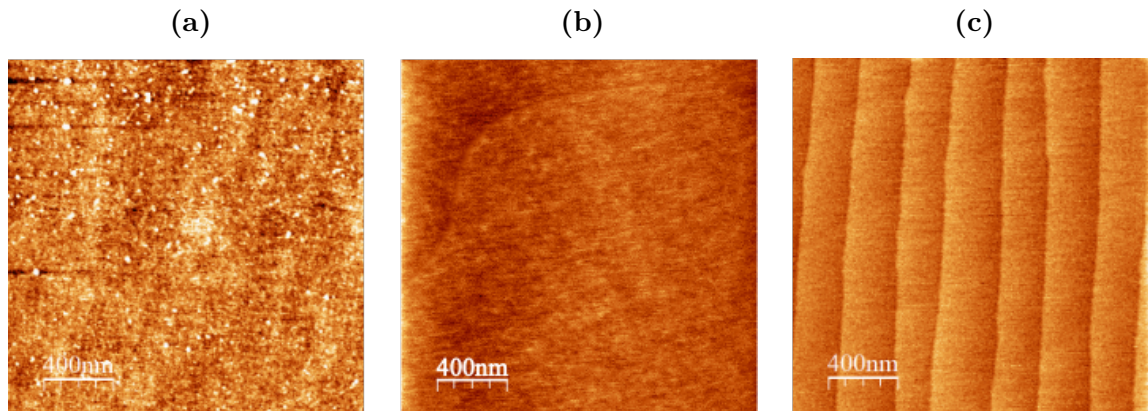


**Fig. 4.1:** AFM image of Al<sub>2</sub>O<sub>3</sub> sunstrates **(a)** as received form Crystec, **(b)** after modified RCA cleaning of the substrate, and **(c)** after annealing of the cleaned before loading in growth chamber. The chemical cleaning helps in removing all the impurities on the substrate.

materials.

3. Rinse in deionized (DI) water thoroughly and blow with dry nitrogen gas.
4. Heat the substrate in NH<sub>4</sub>OH : H<sub>2</sub>O<sub>2</sub> : H<sub>2</sub>O = 1 : 1 : 5 to about 80°C for 10 minutes NH<sup>4+</sup> in the cleaning solution will complex with heavy metal on the substrate surface to form a soluble metal salts which is removed.
5. Rinse in DI water thoroughly and dry with pure nitrogen gas.
6. Soak the substrate in solution of HCl : H<sub>2</sub>O<sub>2</sub> : H<sub>2</sub>O = 1: 1: 3 at about 80°C for 10 minutes H<sup>+</sup> ion in the cleaning solution will replace with the light metal impurities to form soluble salt and be removed.
7. Rinse in DI water thoroughly and dry with pure nitrogen gas.
8. Clean in H<sub>2</sub>SO<sub>4</sub> : H<sub>3</sub>PO<sub>4</sub> = 1 : 3 at about 80°C for 10min to move the oxide layer on the sapphire substrate
9. Rinse in DI water thoroughly and dry with pure nitrogen gas.
10. After drying the sapphire substrate anneal at 1200°C for 4h preferably, but not necessarily, in the O<sub>2</sub> atmosphere.

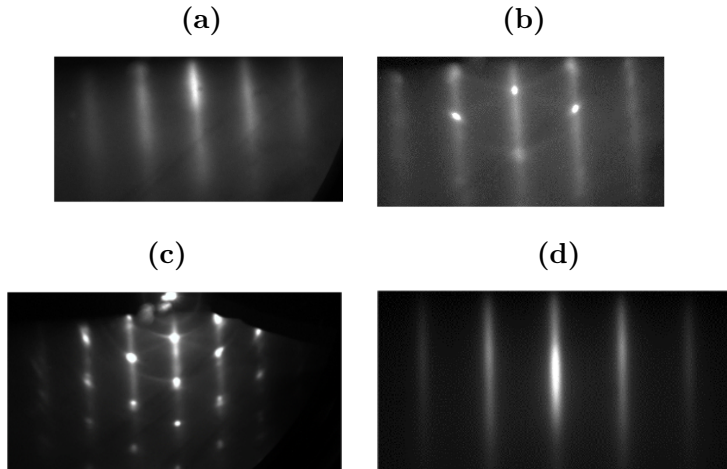


**Fig. 4.2:** RHEED in  $[10\bar{1}0]$  direction of  $NbSe_2$  (a) when growing interfacial layer at  $570^\circ C$ , (b) when growing interfacial layer at  $650^\circ C$ , (c) when continuing growth at  $570^\circ C$  for  $> 2$  h, and (d) when growing interfacial layer at  $570^\circ C$  and continuing the growth at  $650^\circ C$ .

We are able to get rid of the impurities after chemically cleaning it as can be seen in ???. The terraces of the substrate are visible in ?? after annealing it in  $O_2$  atmosphere. The width of the terraces is dependent on the miscut angle of the substrate. Lower the miscut angle, wider the terraces. The cleaned substrate was then loaded into the selenide chamber of PAPAYA where it was first degassed at  $700^\circ C$  for about 1 hour. The substrate surface is now ready for growth of  $NbSe_2$ .

## 4.2 Crystallinity of $NbSe_2$

The growth of any thin film using MBE can be affected by two major factors:

1. temperature of the substrate and
2. flux ratio of the elements of the film

I will discuss their effect on growth of  $NbSe_2$  film one by one.

99.999% pure Nb was evaporated using an e-beam cell and Se was evaporated using K-cell with a flux ratio  $> 1:20$ . The interfacial layer of  $NbSe_2$  grows best around  $570 \pm 20$   $10^\circ C$ . When the temperature  $< 500^\circ C$ , we get polycrystal sample and when the temperature  $> 650^\circ C$  the island growth starts. But

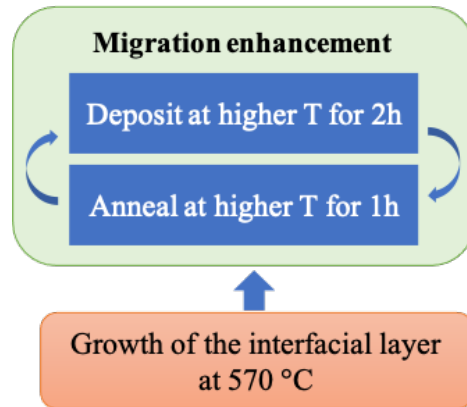


**Fig. 4.3:** Algorithm for growth of NbSe<sub>2</sub>

the subsequent layers do not grow well at the same temperature. In order to avoid, stranski-Krostanov growth all the subsequent layers must be grown at  $650 \pm 20$  10°C. The first 3 monolayer (ML) is grown at  $570 \pm 20$  10°C and all the subsequent layers are grown at  $650 \pm 20$  10°C ?? and ?. The deposited sample is annealed at  $700 \pm 20$  10°C for the first time after deposition of 3 ML and then intermittently after every 10-15 ML.

Long streaky RHEED patterns of the (0001) Al<sub>2</sub>O<sub>3</sub> in [10̄10] and [11̄20] directions were observed indicating a flat and crystalline substrate surface (?? and ??). As the growth of forst monolayer completes the RHEED appears a bit diffused(?? and ??) but as the growth progresses the patter becomse streakier (?? and ??).It means that the grain size increases as the film grows thicker because of increased coalescence. The in-plane lattice parameter for this film is estimated to be  $3.46 \pm 0.03$  Å using RHEED.

As mentioned above the flux of the Nb is many times higher than that of Se; it means that the rate of growth is determined entirely the Nb flux. If we increase the flux of Nb to more than 40 nA, the growth enters into island growth mode very quickly. This is because that the molecuar species do not have enough time to diffuse on the surface of the sample. This flux corresponds to growth rate of 10 MLs/hour. This means that achieving thicker samples is a bit challenging.

Once the sample is taken out from the chamber, its crystallinity is assesed using XRD. We find no spurious peaks between 20 ° and 90 ° range. The standard  $\theta - 2\theta$  X-Ray diffraction (XRD) scan shows that the NbSe<sub>2</sub> film is oriented along (0001) plane with out-of-plane lattice parameter as  $12.77 \pm 0.16$  Å (see ??).

## 4.2 Crystallinity of $NbSe_2$

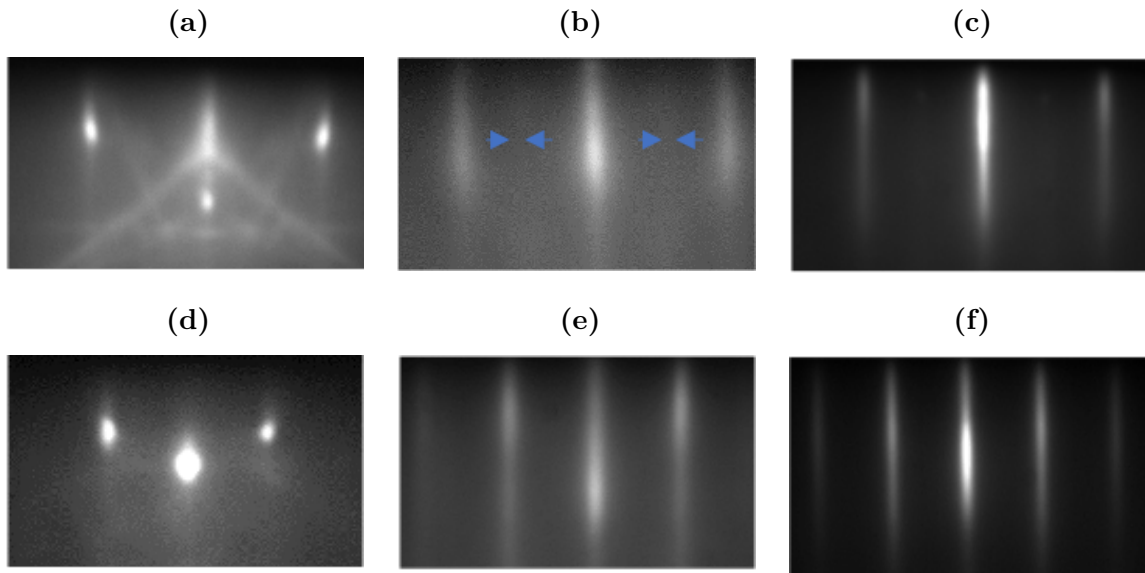


**Fig. 4.4:** The evolution of RHEED image of  $[10\bar{1}0]$  direction of (a) substrate:  $Al_2O_3$ , (b) interfacial layer of  $NbSe_2$  and, (c)  $NbSe_2$  after 6h growth. After rotating the sample by  $30^\circ$ , we observe  $[11\bar{2}0]$  direction of (d) substrate , (e) interfacial  $NbSe_2$ , (f)  $NbSe_2$  after 6h growth.

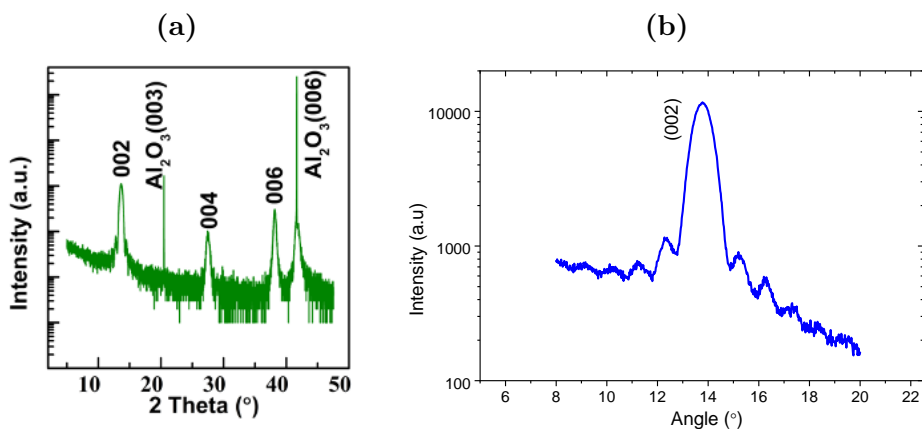


**Fig. 4.5:** X-Ray Difrraction of  $NbSe_2$  (a) full range, (b) (002) peak.

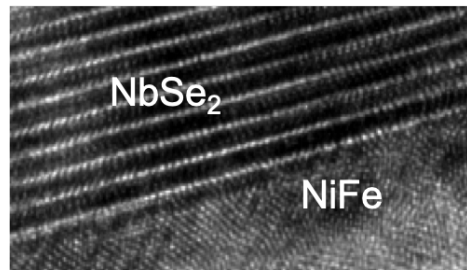


**Fig. 4.6:** TEM micrograph of NbSe<sub>2</sub>

High resolution transmission electron Microscopy image (shown in ??) shows that there is some disorder in the interfacial layer but the the sample grows thicker the the order in the film increases. The planes of the NbSe<sub>2</sub>throughout the film thickness indicating high crystalline order, whereas the ones at the interface with the substrate are a bit corrugated.

### 4.3 Morphology and stoichiometry of NbSe<sub>2</sub>

The STM image shows that the grain size of the film increases with increasing thickness of the film. As the film thickness increases from 4 ML to 8 ML to 15 ML, the grain size keeps increasing as seen in ?. It shows that as the growth progresses the smaller domains coalesce to form larger ones. The atomic resolution in the inset of ?? shows that there are some Se vacancies in the the film. The height scan from one grain (see ??) to another shows  $6.4 \pm 0.1$  Å which corresponds to half the unit-cell height of NbSe<sub>2</sub>.

The sample is completely impurity free because we do not see any spurious peak in the XPS and is perfectly stoichiometric (Nb:Se = 1:2) (see ??)

#### 4.3 Morphology and stoichiometry of NbSe<sub>2</sub>

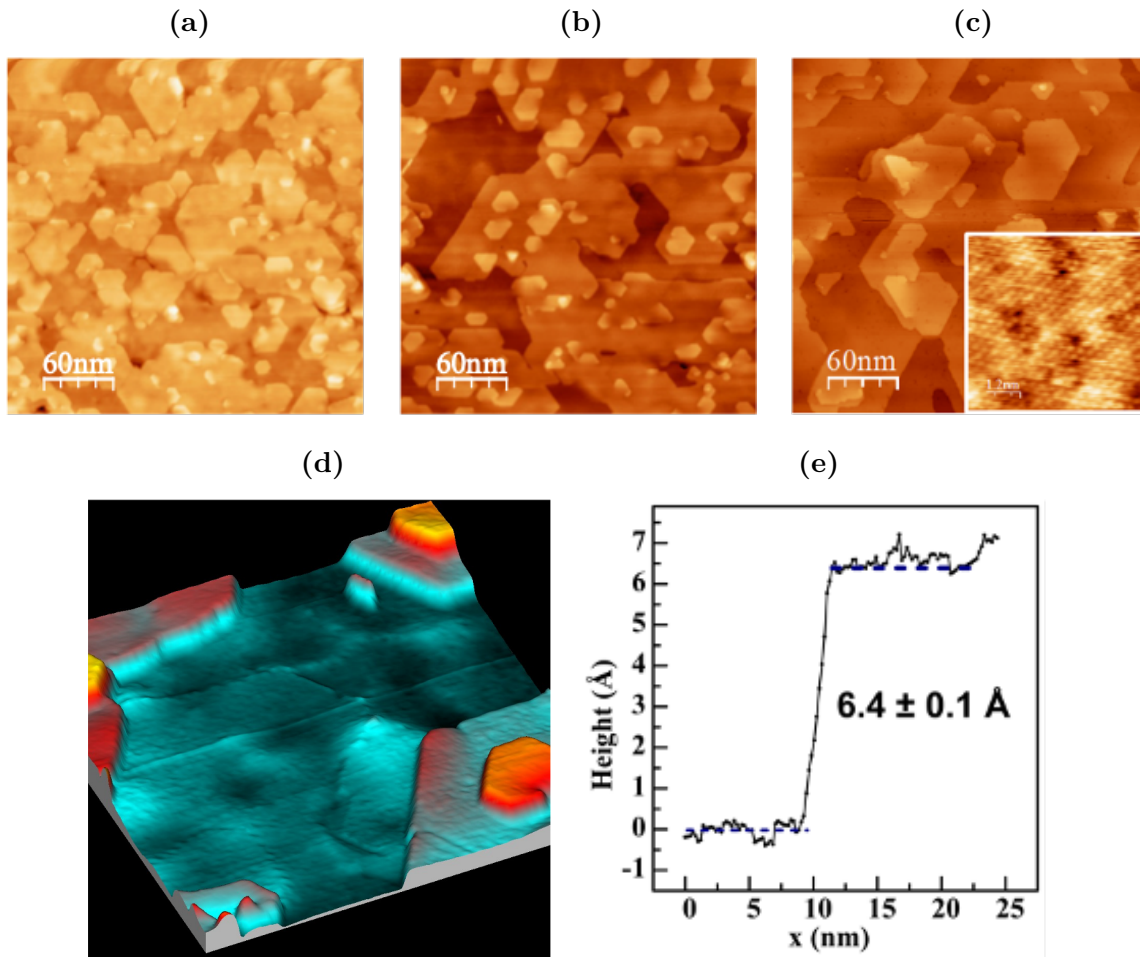


**Fig. 4.7:** STM image of NbSe<sub>2</sub> (a) 4 ML, (b) 8 ML, (c) 15 ML. (d) 3D STM image of NbSe<sub>2</sub>. (e) Step height of NbSe<sub>2</sub>

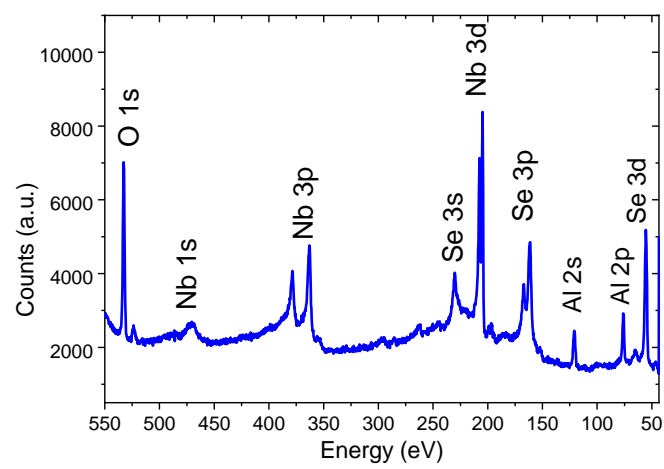


Fig. 4.8: XPS Spectra of  $\text{NbSe}_2$

# 5

## Growth and Characterization of Weyl Semimetals

Weyl semimetals in this study were grown using Molecular beam epitaxy (MBE) on c-plane of MgO substrate from Crystec. The substrate was cleaned using methanol as described in ?? and loaded in TAMARIND where it was degassed at 550°C for about 1 hour. Nb(Ta) and P are co evaoparoated from e-beam and K-cells respectively such that ther flx ratio is 1:20. The growth is monitored continuously using RHEED and the stoichiometry and morphology is assessed intermittently using XPS. Once the sample is taken out of the chamber its structure is assessed using XRD.

### 5.1 Choice of Substrate

The choice of substrate which is lattice matched to Nb(Ta)P is a bit limited by the fact that we need insulating substrate for fabricating electrical and

Material	NbP[100]	TaP[100]	Nb[110]	Ta[110]	MgO[110]
Lattice Parameter (Å)	3.33	3.34	3.30	3.30	3.03

**Table 5.1:** Lattice parameters of different materials in the plane of interest

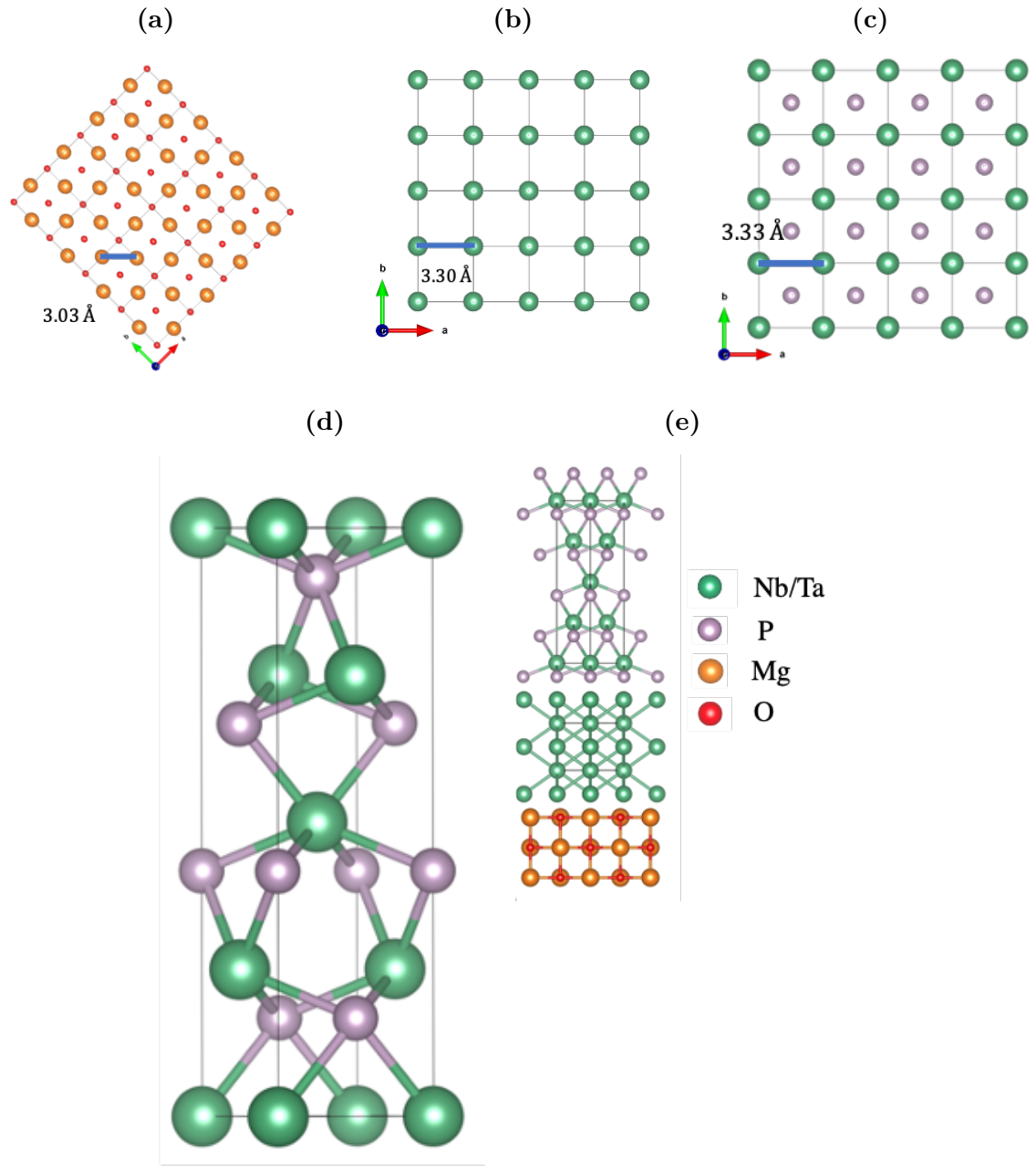


**Fig. 5.1:** Lattice structure of (a) (100) plane of MgO rotated by 45 °for clarity, (b) (100) plane of Nb(Ta), (c) (100) plane of Nb(Ta)P. (d) Nb(Ta)P unit cell (e) Nb(Ta)P/Nb(Ta)/MgO unit cell,

## 5.2 Substrate Preparation

spintronic devices. MgO is one such substrate which can easily be treated to become atomically flat and is lattice matched to [100] direction of NbP with [110] direction in the substrate as shown in ?? and tabulated in ??

### 5.2 Substrate Preparation

Nb(Ta)P were grown in TAMARIND using MBE on MgO substrates, usually 5(×)10 mm in size from the supplier Crystec. The substrate was prepared for growth as follows:

1. Soak the substrate in methanol for 20 minutes.
2. Rinse thoroughly in deionized (DI) water thoroughly and blow with dry nitrogen gas.
3. Anneal the substrate in O<sub>2</sub> atmosphere at 1050 - 1100°C for 3 h.

The process is not fully reproducible. Most of the times we would get atomically flat substrates but occasionally we would see pits and sometimes the terrace are not of atomic step height. The representative figure of both such scenarios have been shown in ?? and ?? with their line scans shown ?? and ??

### 5.3 Evaporation of materials

Ta(Nb) is evaporated from a rod using electron-beam heating and P is evaporated using a GaP effusion cell at 850°C in TAMARIND chamber. The residual P in the chamber sticks to the chamber in two major allotropic forms, *P*<sub>2</sub>(red Phosphorous) and *P*<sub>4</sub>(white phosphorous). The red phosphorus is thermodynamically stable at room temperature but white phosphorous can spontaneously combust at room temperature and turn in lethal phosphine PH<sub>3</sub>gas. Therefore, it is absolutely necessary to keep the white phosphorus concentration to as low value as possible. We observe that the ration of *P*<sub>2</sub>: *P*<sub>4</sub>is around 1:100.

### 5.4 Growth of Nb(Ta)P

There is more than 10% mismatch between the lattice parameters of Nb(Ta)P and MgO. If we try to grow these compounds directly on the substrate, the

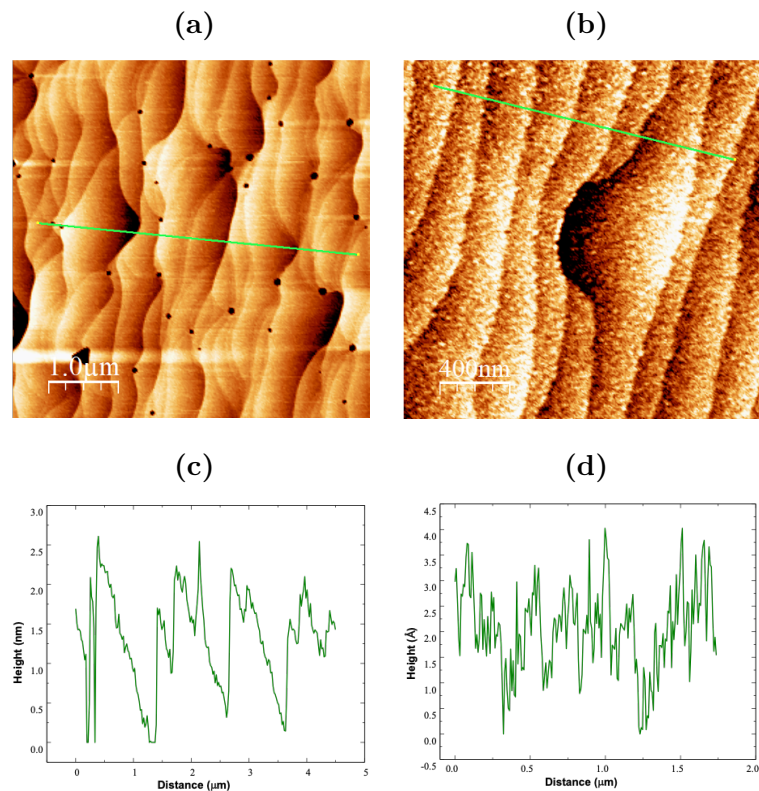


**Fig. 5.2:** AFM of an MgO substrate (a) with pits after cleaning, (b) typical usable sample. Step scan of the substarte (c) with pits after cleaning, (d) typical usable sample.

## 5.5 Structure of Weyl NbP and TaP

film does not remain crystalline; we start getting islands of these films instead of single crystalline flat films. It turns out that if we grow a buffer layer of Nb(Ta) before the growth of phosphide, we get high quality single crystalline films. This buffer layer is grown at 300 °C, at a rate of 3-5 nm/h and a pressure of  $4 \times 10^{-10}$  mbar. The surface of the buffer layer is then exposed to a P2 flux (BEP:  $1 \times 10^{-8}$  mbar) to achieve phosphorization. Once the buffer layer has been phosphorized the surface is ready for growth of Nb(Ta)P. The substrate temperature is maintained between 300 to 400 °C and the film is grown at a slow rate of < 4 nm/h which is limited by the Nb (Ta) flux. The P flux is at least 20 times higher than the Nb flux and has BEP of  $1 \times 10^{-8}$  mbar. The sample is cooled down at the rate of 10 °C/min in P-atmosphere, to ensure that P-termination surface is homogeneous.

### 5.5 Structure of Weyl NbP and TaP

The film quality is constantly monitored using in-situ reflection high energy electron diffraction (RHEED) with 15 kV energy and 1.5 mA filament current. We take an atomically flat terraced MgO substrate (?? and ??) and grow a Nb (Ta) buffer layer on it in order to minimize the lattice mismatch. These layers are rotated 45° with respect to each other i.e. [100] direction of MgO points along the (110) plane of Nb (Ta) as seen in ?? and ?. Before starting the growth of Nb(Ta)P we phosphorize the surface in order to minimize the thickness of the buffer layer. The higher order streaks appear during this process and the RHEED pattern becomes a bit more diffusive as shown in ?? and ?. It suggests that the grain size is not very large yet. Once the growth starts and grains start to coalesce the RHEED pattern becomes very streaky which suggests that the film starts to follow the terraces of the substrate. The periodic RHEED reflections are only visible in the high symmetry directions (45° periodicity), while there are no coherent patterns at intermediate angles, indicating that the NbP (TaP) films grow with a single-crystalline orientation without twinning/twisting of in-plane crystalline domains (?? and ??).

A standard -2 scan taken on NbP films of various thicknesses (9-70 nm) shows only (004) and (008) NbP reflections (Fig. 2a), confirming an epitaxial, single crystalline oriented growth without secondary phases. In order to compare the quantification using both local and global methods, a reciprocal space mapping (RSM) scan has been performed on the (1,1,10) reflection of NbP (Fig. 2d),

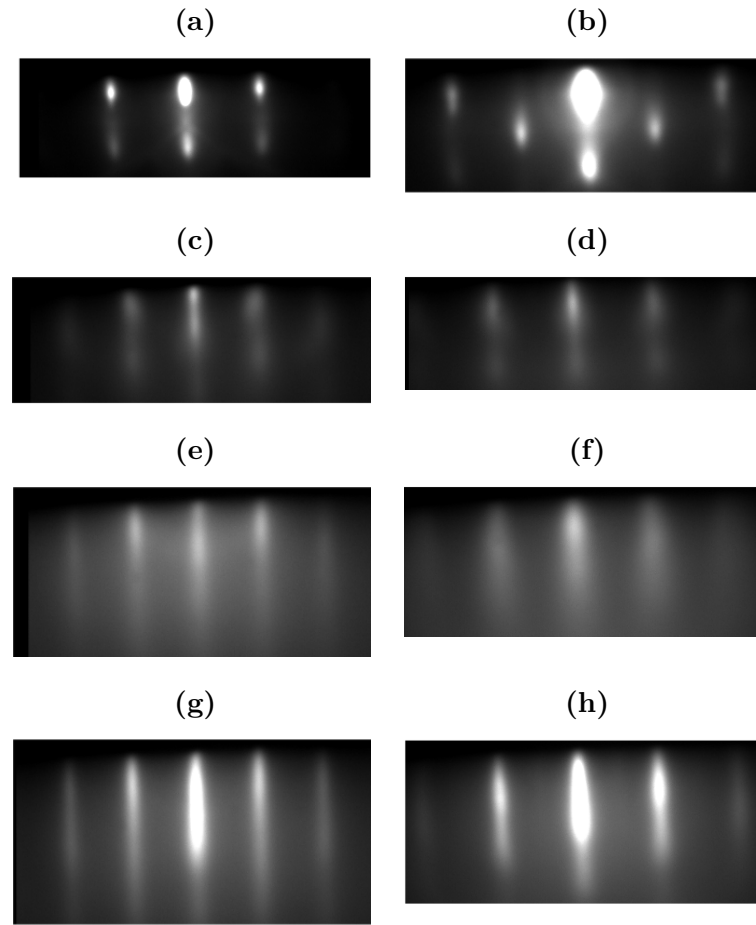


**Fig. 5.3:** MgO substrate before growth in (a) [100] (b) [110]. Nb buffer layer in (c) [100] (d) [110]. Nb buffer layer after phosphorization in (e) [100] (f) [110]. NbP thin film in (g) [100] (g) [110].

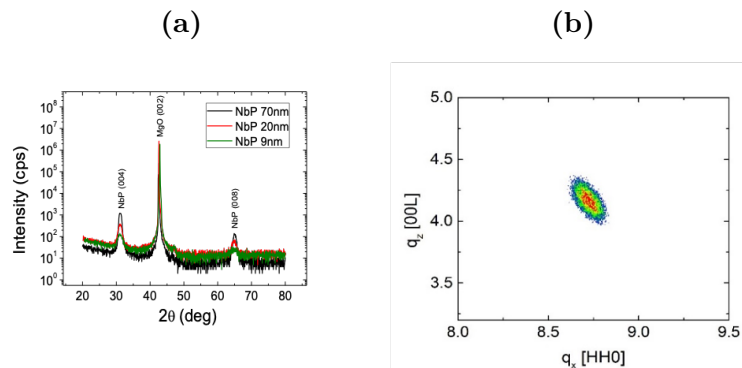


**Fig. 5.4:** (a) Theta-2Theta Scan and (b) RSM scan of NbP.

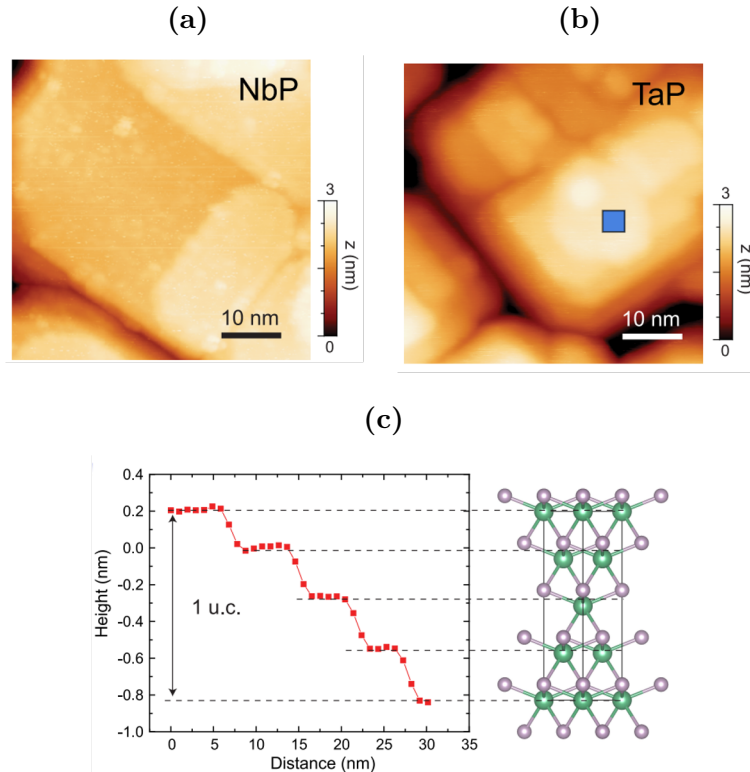


**Fig. 5.5:** (a) AFM of NbP and (b) AFM of TaP. (c) Line Scan of NbP

yielding an in-plane lattice parameter of  $a = 3.391\text{\AA}$ . The in-plane lattice parameters do not vary from as the thickness is varied from 15nm to 70nm according to the RSM measurements (see Sup. Fig S2), which means that the films do not change the in-plane strain state in the studied thickness range. On the other hand, the out-of-plane lattice parameters extracted from the (004) peak positions (inset of Fig. 2a) decrease only very slightly ( $11.50\text{\AA}$  to  $11.46\text{\AA}$ ) with increasing thickness. The negligible thickness dependence of both in-plane and out of-plane parameters suggest that the films grow fully relaxed from the very early stage. Interestingly, the lattice parameters ( $a = 3.39\text{\AA}, c = 11.48\text{\AA}$ ) sizably differ from the bulk values ( $a = 3.34\text{\AA}, c = 11.37\text{\AA}$ ), which means that a bigger unit cell is stabilized during the layer-by-layer growth on the MgO(001)/Nb(001) surface.

## 5.6 Morphology of TaP and NbP

The topography and surface structure of NbP and TaP films is of paramount importance for the observation of topological surface states (Fermi-arcs) and was thus investigated by scanning probe microscopy (Figure 4 and Supp. Fig S5). Large-scale atomic force microscopy images (Supp Fig. 5a) reveal a flat topography, yielding root mean square (RMS) roughness values of 0.43 nm. The grain size varies from 50 to 100 nm showing regions of grain coalescence, whereas the inter-grain steps correspond mostly to 1 unit cell height. In order to investigate the topography inside and between the grains, in-situ scanning tunneling microscopy images have been acquired (Figure 4). Square- and rectangular shaped grains can be identified with two preferred orientations, along  $45^\circ$  and  $-45^\circ$  on the image axis (i.e. along (100) direction), consistent with the four-fold in-plane crystal symmetry of NbP. A closer look to the grain topography reveals the presence of atomically flat terraces. The height of each step terrace amounts to 2.8 Å, corresponding to  $\frac{1}{4}$  unit cell fractions (a single Nb-P monolayer), as depicted in Figure 2b (a structural model of the NbP unit cell along the growth direction (001) is drawn as guide to the eye). We rarely find slight deviations of exact unit cell fractions, which might arise if adjacent grains end in a different (Nb / P) atomic termination or due to the presence of inter-grain stacking faults. From the topography statistics, a predominantly single surface termination (either Nb or P) scenario is likely to happen throughout the film surface. Figure 4c and 4d show a zoomed-in topography image comparing NbP and TaP film surfaces, the latter having a smaller terrace width.

## 5.7 Stoichiometry of Weyl Semimetals

The chemical composition and valence states of the NbP (TaP) thin films have been studied by in-situ X-ray photoemission spectroscopy (XPS) and ex-situ Rutherford backscattering spectroscopy (RBS). The Nb 3d 5/2 and P 2p core level peaks in XPS spectra is shown in ???. The figure shows that Nb and P peaks shift in opposite directions compared to the neutral Nb<sub>0</sub> and P<sub>0</sub> valence state. This is consistent with the expected chemical shifts due to electron transfer in the NbP compound (Nb<sup>III</sup> and P<sup>V</sup> valence). The stoichiometry of the films has been determined using equation (37), yielding a slightly P-rich

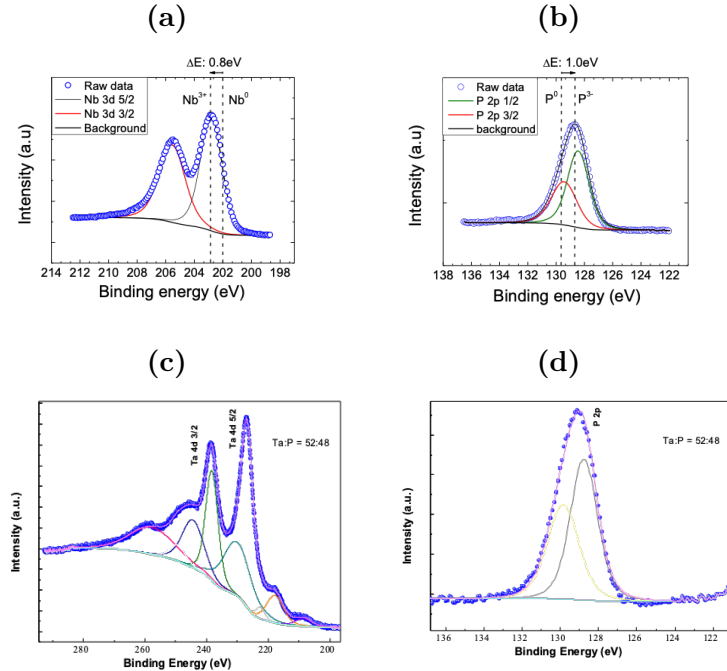


**Fig. 5.6:** (a) Nb 3d peak and (b) P 2p peak in NbP. (c) Ta 3d peak and (d) P 2p peak in TaP.

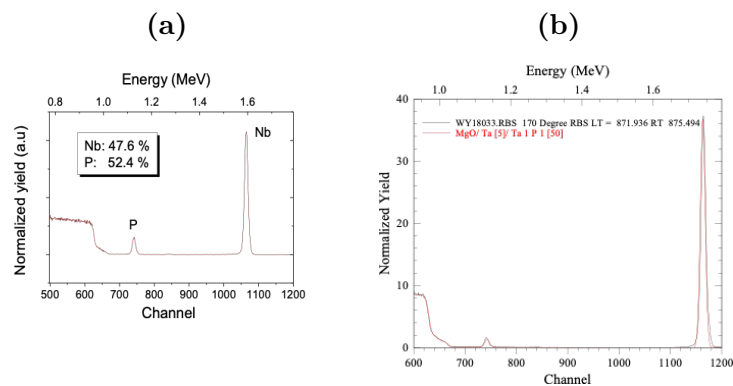


**Fig. 5.7:** RBS spectra of (a) NbP (b) TaP.

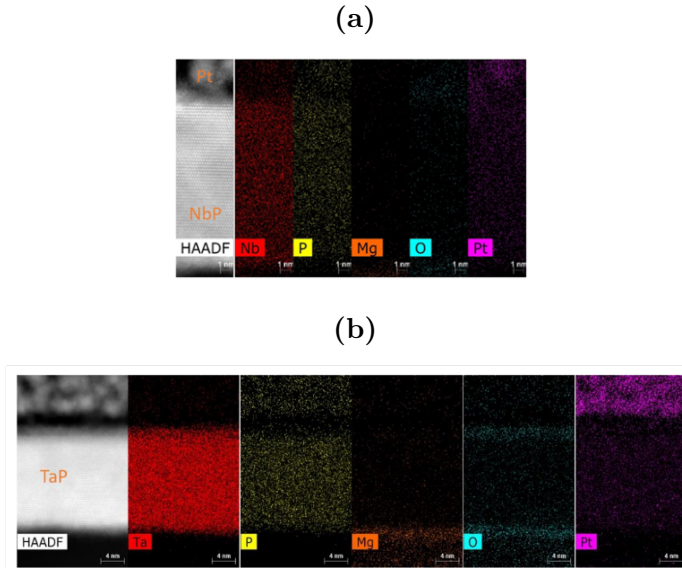


**Fig. 5.8:** EDX Spectra of (a) NbP (b) TaP.

(Nb<sub>0.49</sub>P<sub>0.51</sub>) composition. In addition to XPS, which is a surface sensitive technique, the in-depth composition of the films has been studied by Rutherford backscattering spectroscopy (RBS). The best fitting to the spectra ??, yields a 47.6% to 52.4% (Nb:P) composition, indicating that the P-rich composition is distributed homogeneously across the full NbP layer. Similar results with regard to bonding-related core-level shifts and P-rich composition have been found in TaP layers which are shown in the same figure. A real-space visualization of the layer homogeneity is further shown by energy-dispersive X-ray spectroscopy along a NbP and TaP cross section is shown in ??.

The fine details of the structure are shown in Figure 2c, where a high-resolution high-angle annular dark field (HAADF) STEM image of the NbP in the [110] direction displays highly-ordered in-and out-of-plane lattice planes, with an excellent matching to the NbP structural model. The lattice planes are particularly visible by the high atomic contrast of the Nb atoms, while a faint contrast corresponding to the light P atoms can be distinguished in the zoomed-in image (Figure 2c, right panel) at the expected atomic positions. Taking advantage of the excellent structural order, a line intensity profile of the atomic rows has been taken to calculate the average in-plane lattice parameter of the NbP film (Supp. Figure S1). For the [110] direction, a Nb-Nb atom distance of 2.40 Å has been inferred, which results in an in-plane lattice parameter  $a = 3.394 \text{ \AA}$ .

## 5.8 Reciprocal space characterization of NbP

Having assessed the properties of the film surface, momentum-resolved photoemission spectra have been taken using an in-house designed and built momentum microscope<sup>45</sup> with a He-I light source. Figure 5 summarizes the overall electronic structure of a 15 nm-thick NbP thin film measured at 100K, including Fermi-surface topology and band dispersion along relevant (Weyl point) cuts, together with ab-initio calculations using the experimentally obtained unit cell parameters. At the Fermi-energy, four electronic pockets with an elliptic shape directed towards the X and Y symmetry points can be identified, as shown in Fig. 5a. A detailed comparison with the calculation of the termination-dependent surface states (Figures 5b and 5c) reveal that the elliptic and cross-like band features along -X and -Y are characteristic of the P-terminated NbP surface states (the features for a Nb-termination are radically different). Interestingly, the size and shape of the measured elliptical (also called spoon-like) features match with the calculations and the bulk crystal data in Refs.<sup>10,11,46</sup> only when an energy shift of  $\Delta E = 0.2\text{eV}$ . is considered (highlighted in a green box, Figure 5b), suggesting an effective hole doping in the as-grown thin films. Figure 5d shows the energy dispersion cut along  $A \rightarrow A'$ , which is expected to cross the location of one pair of Weyl-points in NbP ( $k_x = 0.54\text{\AA}^{-1}$ ,  $E_b = -0.026\text{eV}$ ) and thus used to visualize the surface Fermi arcs. A clear linear band dispersion is observed, in agreement with previous photoemission results of cleaved monopnictide bulk crystals.<sup>6-11</sup> This dispersion originates from the Fermi-arcs, but their  $k_x$ - $k_y$  contour at the Weyl points cannot be mapped in our NbP films due to the EF shift (-0.2 eV) with respect to the intrinsic Fermi-level, and secondly, due the intrinsically short separation of the Weyl points in momentum space ( $< 0.05\text{\AA}^{-1}$ ), a detection challenge even for high-resolution synchrotron ARPES. It is noteworthy that only these topological surface states (elliptic shape,  $A \rightarrow A'$  cut) are observed in our films, whereas the bowtie features centered at the X and Y points) are completely absent. This merits further investigation and will be discussed elsewhere. On the other hand, the origin of the effective hole-doping in the as-grown thin films can be attributed to residual acceptors (Nb-vacancies) arising from the MBE growth process, in agreement with the slightly P-rich composition of the films inferred by XPS and RBS. The strained lattice parameters of the phosphide thin films will also have an effect on the Fermi-level position. Although we estimate that the effect of the lattice parameters ( 1% tensile strain) is rather small, further studies are needed

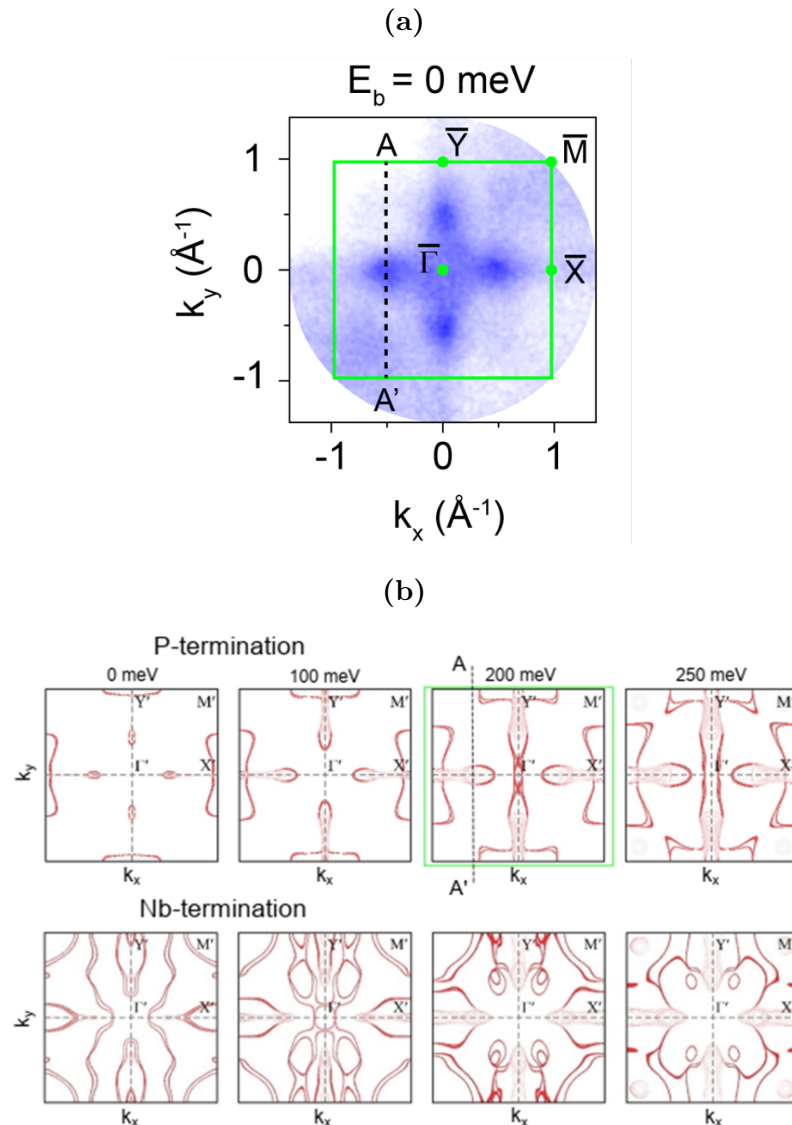


**Fig. 5.9:** (a) Calculated fermi surface of NbP. (b) Measured fermi surface of NbP

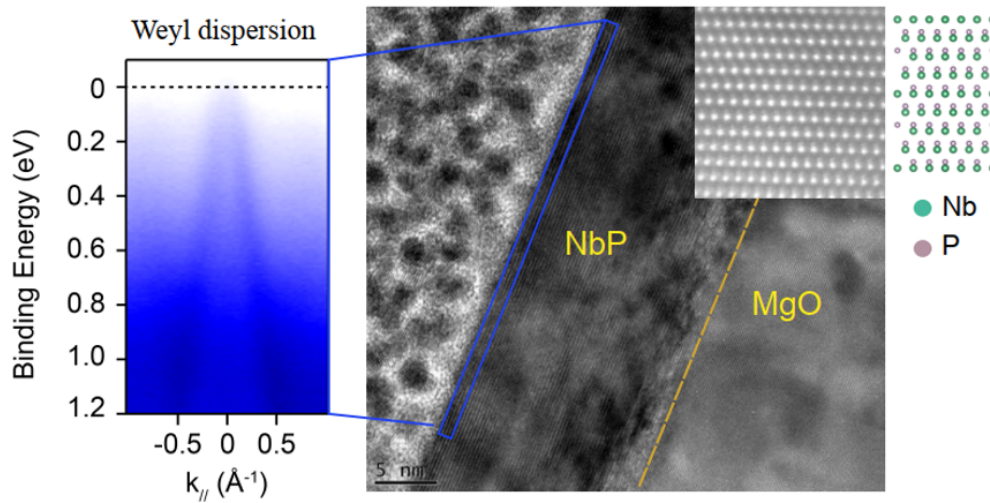


**Fig. 5.10:** TEM and ARPES of NbP

to disentangle the contribution from strain and vacancy acceptors on EF, in order to get a full understanding of Fermi-level engineering of Weyl semimetals achieved by epitaxial design.



# 6

## **Electrical Properties of Quantum Materials**

**6.1 Electrical Properties of NbSe<sub>2</sub>**

**6.2 Electrical Properties of Weyl Semimetals**



# 7

## Spin to Charge Conversion

**7.1 STFMR of  $\text{NbSe}_2$**

**7.2 Second Harmonic Hall of  $\text{NbSe}_2$**

**7.3 STFMR of  $\text{NbSe}_2$**

**7.4 Second Harmonic of Weyl Semimetals**

**7.5 Comparison of different materials**



# **Eidesstattliche Erklaerung (Statutory declaration)**

Hiermit erkläre ich, Avanindra Kumar Pandeya, die vorliegende Arbeit, Epitaxial thin

I have written the present work, Quantum materials for spin to charge conversion, independently and without third-party help. No sources other than those cited by me were used. Elements quoting directly from, or making reference to, such sources have been identified as such. I declare that I have provided this information truthfully, that I have not made any previous unsuccessful attempts at doctoral studies, and that I have not submitted either the current version or another version of this thesis to another academic institution for the purpose of obtaining an academic degree. I do not have any prior criminal convictions, nor am I subject to any preliminary investigations.

Halle (Saale), Avanindra Kumar Pandeya



# Acknowledgements

I would like to thank Prof Stuart Parkin for the opportunity to undertake my doctoral studies under his supervision, and for his valuable expertise and guidance during my time at the Max Planck Institute of Microstructure Physics. Here, my gratitude goes to the many other scientists and students, foremost Edouard Lesne, for their advice and encouragement in my development as a scientist: Fasil Kidane Dejene, Kumari Gaurav Rana, Neeraj Kumar, Peter Werner, Hakan Deniz, Hoelger Meyerheim, Robin Blaesing, Pranava Keerthi Sivakumar, Elisa Yang, Amilcar Bedoya Pinto, Avanindra Kumar Pandeya, Tianping Ma, Bharat Grover, Binoy Krishna Hazra, Banabir Pal, Hao Yang, Jue Huang, Yicheng Guan, Ankit Kumar Sharma, Abhay Kant Srivastava, Jibo Zhang, Jae-Chun Jeon, Andrea Migliorini, Kai-Uwe Demasius, Elena Derunova, Mazhar Ali, Amir Capua, Rana Saha, Bin Cui, Fang Gao, Ajaya Nayak, Ilya Kostanovski and, of course, Jiho Yoon, Alessandro Fumarola and Amine Wahada. For technical assistance, I heartily acknowledge Kai-Uwe Assmann, Kornelia Sklarek, Martin Gottschalk, Norbert Schammelt, Mike Borrmann and Pierre-Jean Zermattan, as well as the wisdom of Winfried Heichler. For administrative help over the last few years, my thanks go to Antje Paetzold and Simone Jaeger.